Three S_0/S_1 Conical Intersections Control Electron-Transfer-Catalyzed Chemiluminescence of 1,2-Dioxetanedione

Ling Yue* and Ya-Jun Liu*

Read Online

ACCESS | Metrics & More | Article Recommendations | Supporting Information

ABSTRACT: Chemiluminescence (CL) utilizing four-membered cyclic peroxides is one of the most useful analytical techniques. Up to now, the CL mechanisms for nonketone (1,2-dioxetanes) and monoketone (1,2-dioxetanones) derivatives of four-membered cyclic peroxides have been intensively studied experimentally and theoretically in the past several decades, but no general mechanism has been concluded to rationalize the origin of high-efficiency singlet chemiexcitation. In contrast, as the only diketone derivative of four-membered cyclic peroxide, the electron-transfer (ET)-catalyzed CL of 1,2-dioxetanedione (DDO), which is most suggested as a critical step in the well-known peroxyoxalate CL (POCL), has never been theoretically investigated and uncovered yet. In this work, we theoretically investigated the rubrene-catalyzed decomposition of DDO for the first time, with a hybrid quantum mechanical/molecular mechanical model and nonadiabatic molecular dynamics simulation. The computation shows a stepwise ET-catalyzed decomposition and three S_0/S_1 conical intersection (CI)-controlled singlet chemiexcitation. The three universal S_0/S_1 CIs play different roles in the high-efficiency singlet chemiexcitation in ET-catalyzed CL of DDO and should be the true origin of the high-efficiency singlet CL. We believe that the current work could not only provide a further understanding for high-efficiency singlet CL but also provide some general clues to designed new high-efficient CL systems.
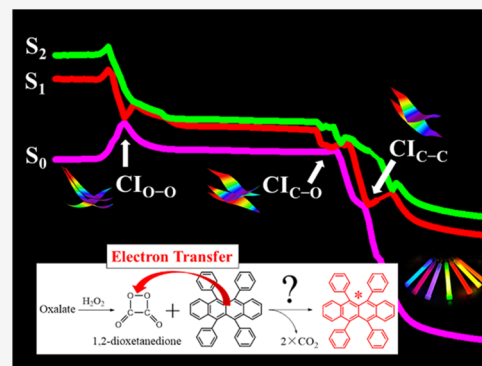
1. INTRODUCTION

Owing to the simplicity and versatility for energy transformation and determination on a wide variety of species, chemiluminescence (CL) is usually acknowledged to be one of the most highly sensitive and most useful analytical techniques.[1−3] In solution, many oxidation reactions that form labile peroxides were found to yield CL,[4−7] and the exothermic decomposition of peroxides especially four-membered cyclic peroxides has nearly formed the basis for nearly all of organic CL.[8] In the past decades, the CL mechanisms of various four-membered cyclic peroxides were studied experimentally[6,9−12] and theoretically.[13−27] Uncatalyzed unimolecular decomposition via a stepwise biradical process is proven to lead to rather low CL yields, thereby not explaining the high CL efficiency. In contrast, the electron-transfer (ET)-catalyzed decomposition of cyclic peroxides discovered by Koo and Schuster[8,28] solves the main shortcomings of the uncatalyzed dissociation: high activation energy and low singlet chemiexcitation yield. ET-catalyzed CL is usually explained by the well-known chemically initiated electron exchange luminescence (CIEEL) mechanism proposed by Schuster and co-workers in the 1970s.[8,29] In addition, the charge-transfer-induced luminescence (CTIL)[23] and the related gradually reversible CTIL[23] (GRCTIL)[30] mechanisms using an incomplete or partial charge transfer (CT) and back CT (BCT) instead of a complete single ET and back ET (BET) are also employed to improve the CIEEL mechanism.

The core idea of ET-catalyzed CL is that an external electron-rich activator (intermolecular ET, Scheme 1A) or an electron-rich group substituted on cyclic peroxide (intramolecular ET, Scheme 1B) acts as an electron donor to catalyze the dissociation of peroxide bonds and enhance the singlet

**Scheme 1. (A) Intermolecular, and (B) Intramolecular ET-Catalyzed Decomposition of Cyclic Peroxides**
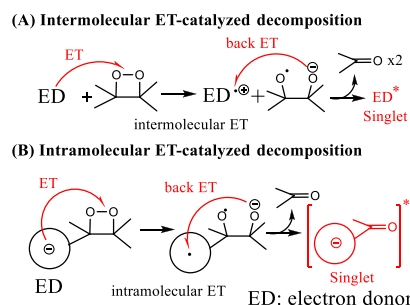
chemiexcitation.[21] No matter in the intramolecular or intermolecular case, a BET (BCT) process is required and considered to be responsible for high-efficiency singlet CL.[21] However, our recent theoretical investigation on luminol CL[31,32] and fungal bioluminescence (BL)[33] shows that the BET (BCT) is not a requirement for high singlet chemiexcitation. This inspires us to review again the origin and nature of the high singlet chemiexcitation in ET-catalyzed CL reaction.

On the other hand, for four-membered cyclic peroxides, three types of parent structures, 1,2-dioxetane, 1,2-dioxetanone, and 1,2-dioxetanedione (Chart 1), are widely discovered in various

Chart 1. Chemical Structures of 1,2-Dioxetane, 1,2-Dioxetanone, and 1,2-Dioxetanedione
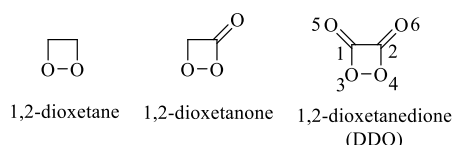
high-efficiency CL and BL reactions. Up to now, the ET-catalyzed CL mechanisms for 1,2-dioxetanes (Scheme 2A)[20] and 1,2-dioxetanones (Scheme 2B)[30] have been studied and revealed by our previous state-of-the-art multireference computations. However, as the only diketone derivative of four-membered cyclic peroxide, the ET-catalyzed CL mechanism for 1,2-dioxetanedione (DDO) has never been theoretically investigated and uncovered yet. Since DDO itself has very weak light emission in the absence of an activator,[34−36] the intermolecular ET-catalyzed decomposition of DDO is most suggested, although not completely proven, as a critical step in the well-known peroxyoxalate CL (POCL). In POCL, the catalyzed oxidation of oxalate esters like bis(2,4,6-trichlorophenyl) oxalate (TCPO, Chart S1) with hydrogen peroxide could yield extremely high light emission (Φ_{CL} can reach 60%)[12,16,37,38] making it to be one of the most efficient CL reactions known and be often utilized in chemical lights ("lightsticks"). Actually, both experimental[12,16] and theoretical[39]

research studies demonstrate that only intramolecular ET-catalyzed CL transformations can occur with high singlet efficiency in general, while the intermolecular ET-catalyzed CL is commonly inefficient. The ET-catalyzed decomposition of DDO is hence a notable exception and successful example for the intermolecular ET-catalyzed CL system.

Therefore, we performed the first theoretical investigation on the rubrene (RUB, Chart S1)-catalyzed decomposition of DDO in an ethyl acetate (EAC) solvent (Scheme 2C) by density functional theory (DFT) and spin-flip time-dependent DFT (SF-TDDFT) combining the hybrid quantum mechanics/molecular mechanics (QM/MM) model and nonadiabatic molecular dynamics (NAMD) simulation. Based on the theoretical simulation, the ET-catalyzed stepwise decomposition and chemiexcitation mechanism of DDO are revealed, and the role of located three S_0/S_1 conical intersections (CIs) and origin of high-efficient singlet chemiexcitation are also discussed.

2. COMPUTATIONAL DETAILS

2.1. Molecular Dynamics. The neutral RUB and DDO fragments are solvated in an ethyl acetate (EAC) box by AmberTools (tleap) with a 40 Å buffer distance. Thus, the RUB and DDO are solvated in a cuboid solvent box with 33,478 EAC molecules. The solvated system was first relaxed via energy minimization. After initial MM optimization, the system was gradually heated to 300 K within 40 ps. Then, additional 40 ps MD was performed to equilibrate the system in an NPT ensemble under 1 atm and 300 K. During the above classical energy minimizations and MD simulations, the whole system is allowed to move freely. After the NPT MD, the final size of the EAC solvent box is about 64/76/80 Å and the final density is 0.89 g/mL.

To determine a RUB−DDO distance for the following QM/MM model, an umbrella sampling[40] along the distance (r) between RUB and DDO is performed with the harmonic constraint potential $V = k(r - r_0)^2$, where r is chosen as the distance between the geometric centers of RUB and DDO. A total of 47 windows are performed for the umbrella samplings constrained with $r_0 = 3.5−8.0$ Å and equal force constants k, 5.0

Scheme 2. Chemiluminescence Mechanisms of Cyclic Peroxides in (A) 3-(2′-Spiroadamantyl)-4-methoxy-4-(3″-phosphoryloxy)-phenyl-1,2-dioxetane (AMPPD) CL, (B) Firefly BL, and (C) POCL Investigated by Previous[20,30,31] and Current Theoretical Works
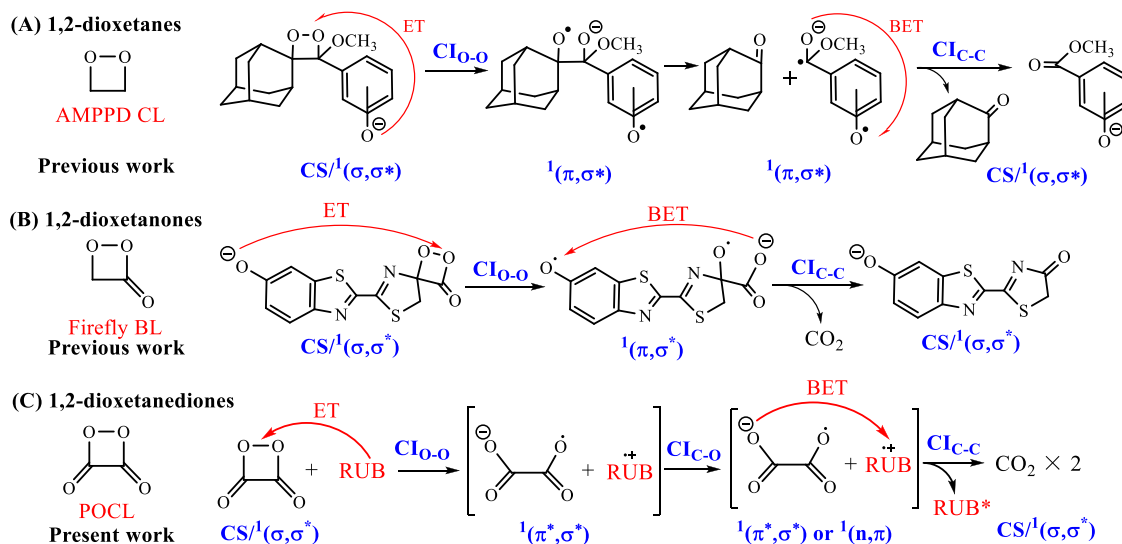
kcal/mol. Initially, NPT runs of MM-MD simulations with umbrella sampling potentials over 50 ps are performed on each windows at 1 atm and 300 K to equilibrate the systems. Then, MM-MD production runs over 100 ps, also in the NPT ensemble and at 1 atm and 300 K, are continued from the final structures after the equilibration. For comparison, gas-phase umbrella samplings are also performed for RUB and DDO using the same approach above.

Finally, the one-dimensional potentials of mean force (PMF) from the umbrella samplings are obtained using the weighted histogram analysis method (WHAM)[41] and plotted in Figure S1. As shown in Figure S1A, in the gas-phase model, a RUB-DDO encounter complex can be observed around $r \approx 5$ Å. In contrast, in EAC solution, the PMF curve of the system slightly increases along with RUB−DDO distance r decreasing from 8.0 to 4.5 Å as shown in Figure S1B. After $r > 4.5$ Å, the free energy increases rapidly, indicating a strongly exclusive interaction between the reactant and catalyst. Although, not a solvent, the caged reactant complex is observed in current simulation, the small free energy (∼0.5 kcal/mol) also indicates a high possibility for the RUB and DDO collision. In principle, both the RUB−DDO distance and the orientation of RUB with respect to DDO might influence the bimolecular reaction. As the role of catalysis RUB in this reaction is providing an electron for the O−O cleavage, the possible influence of the RUB orientation could only be the overlap between the σ orbital of O−O and the π^* orbital of RUB, which might strongly affect the coupling between the diabatic (σ,σ^*) and (π,σ^*) states. In fact, the influence of the orbital overlap probably did not work since the RUB and DDO have a considerable distance (>4.5 Å). Therefore, the orientation of the RUB is not considered in the umbrella sampling, and a random snapshot from the MM-MD trajectory in the window with $r_0 = 4.5$ Å is directly used as the starting point for the following QM/MM calculations.

All the MM optimization, MD simulation, and umbrella sampling are performed by Amber Tools.[42] All the bonded and van der Waals force field parameters are adapted from the general Amber force field (GAFF)[43] for RUB, DDO, and EAC, while the equilibrium bond lengths, bond angles, dihedral angles, and restricted electrostatic potential (RESP) charges are obtained from the optimized geometry at the HF/6-31G* level.

2.2. QM/MM Calculations. For QM/MM computation, a two layer ONIOM (our own n-layered integrated molecular orbital and molecular mechanics) scheme with a mechanical embedding approach is adapted to perform the geometric optimizations for all the critical stationary points on the S_0 surface including the possible local minima (Mins), intermediates (Ints), and transition states (TSs). From the located TSs, the intrinsic reaction coordinate (IRC) calculations are performed within the ONIOM scheme to find out the reaction path connecting Min and Int. To maintain the density of solution (about 0.9 g/mL), all the QM and MM atoms whose distance from the QM atoms is less than 10 Å are relaxed while the other MM atoms are fixed during the geometric optimization and IRC calculations. In addition, the solvent molecules (EAC), which are far from the QM atoms over 25 Å, are removed from QM/MM calculations to save computational resource and time. Thus, a total of 811 EAC molecules are involved in the QM/MM optimized and TSH dynamics.

The high layer of ONIOM, which consists of RUB and DDO, is calculated by DFT with unrestricted open-shell approximation and SF-TDDFT with Tamm/Dancoff approximation (i.e., SF-DFT),[44] while the low layer, which concludes only the explicit solvent molecules, is treated by MM with GAFF. Although, currently, the analytic Hessian at the SF-DFT level is still not available, the frequency analyses and intrinsic reaction coordinates (IRC) on the ground state are hence all using normal DFT while the ground and excited-state singlet point energies are corrected by SF-TDDFT based on the DFT IRC with the ONIOM model. For the excited-state, only the lowest singlet states are considered because the triplet states cannot be described properly in SF-DFT and the excited products are mainly dominated by singlet ones.

In addition, the minimum energy conical intersections (MECI) are optimized at the SF-DFT levels in the gas phase using the branching plane updating (BPUPD)[45] method as the MECI optimization using external energy and gradient is currently not available in Gaussian 16. The initial geometric structures of the MECI optimization were modified from the QM part of ONIOM optimization.

For normal DFT energy and gradient calculations in ONIOM, the Coulomb attenuated hybrid exchange-correlation functional (CAM-B3LYP),[46] which was designed to describe CT excitations, is used, while the BHHLYP functional[47] (50% Hartree−Fock + 50% Becke for exchange and LYP for correlation) is selected in all SF-DFT calculations. Broken-symmetry (BS) technology is adopted in the unrestricted open-shell ground state in CAM-B3LYP calculations. The 6-31G** basis set is employed for all the DFT and SF-DFT calculations. The larger basis sets with the diffusion functional have been tested and showed no improvement in the geometry optimization (see Table S1 and Figure S2). All the ONIOM optimization, vibrational analysis, and IRC calculations are finished using the Gaussian 16 program suite,[48] while the energies and gradients of SF-DFT are obtained from the US variant of general atomic and molecular electronic structure system (GAMESS-US) via the external interface provided by Gaussian 16. The derivative coupling vectors (DCV) and gradient difference vectors (GDV) at the SF-DFT level are calculated by Q-Chem.[49]

2.3. QM/MM On-the-Fly Trajectory Surface Hopping Dynamics. The RUB-catalyzed chemiluminescence decomposition of DDO is investigated by on-the-fly trajectory surface hopping (TSH) dynamics[50,51] in the framework of the Zhu−Nakamura algorithm with global switching probability.[52−56] A total of 600 random velocities are sampled at a constant temperature of 300 K as an initial condition based on the first transition states $(TS_{O−O})$ optimized at the ONIOM(CAM-B3LYP/6-31G**:GAFF) level, according to the algorithm proposed by Sellner et al.[57] First, the random initial velocities are created. Then, the translational and rotational velocities are removed by transforming the system into a center-of-mass coordinate. Finally, the velocities are rescaled to give the required initial kinetic energy. In current simulation, the zero-point vibrational energy, 425.0 eV, calculated at the ONIOM level is chosen as the initial kinetic energy. Thus, the statistical behavior of the trajectories can be described by the canonical (NVT) ensemble. The nuclear motion of all atoms is treated as classical particles, by numerical integration of Newton's equations of motion, and all nuclear coordinates are taken into account. Newton's equations are integrated using the velocity Verlet algorithm[58−60] with a constant time step of 0.5 fs and a maximum simulation time of 1 ps. The criterion for the total energy conservation is set to the default value (0.5 eV) in Newton-X. The trajectories are forced to be terminated if the O−O and C−C distances are both larger than 5.0 Å. The lowest
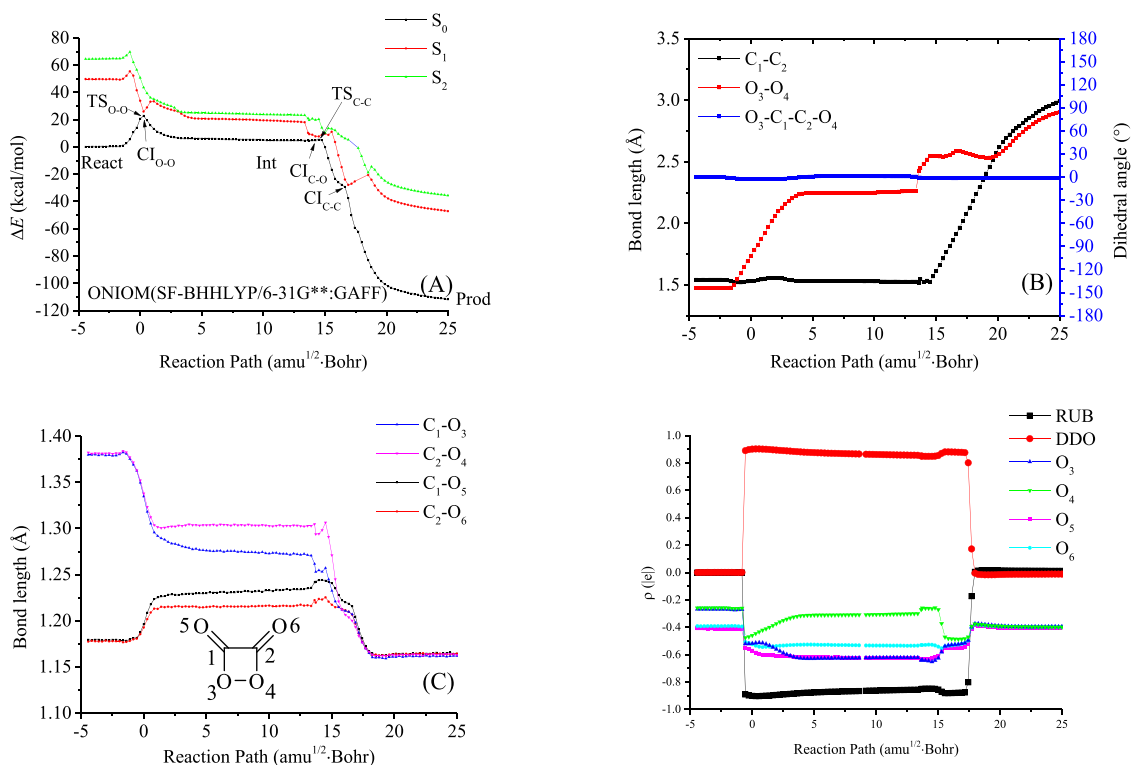
Figure 1. (A) Adiabatic S_0, S_1, and S_2 PECs, (B) C_1-C_2, O_3-O_4 bond lengths, and $O_3-C_1-C_2-O_4$ dihedral angles, (C) four C−O bond lengths, and (D) Mlliken charge populations along the reaction path at the ONIOM(SF-BHHLYP/6-31G**:GAFF)//ONIOM(CAM-B3LYP/6-31G**:GAFF) level.

four singlet states are involved in TSH simulation, and on-the-fly switching probability between them is computed by the Zhu−Nakamura algorithm.

The multireference configuration interactions (MRCI) with semiempirical Hamiltonion OM2, AM1, PM3, and MNDO are all benchmarked as shown in Figure S3. The PECs by the ONIOM(MNDO/MRCI:GAFF) with 8 active electrons and 10 orbitals show the best performance for the ground and exited PECs along the reaction path in comparison to taking the PECs by ONIOM(SF-BHHLYP/6-31G**) as a reference. Thus, it is used in on-the-fly calculations of the potential energies and nuclear gradients required by the TSH simulation. The QM/MM TSH dynamics with the Zhu−Nakamura algorithm are implemented in our newly modified Newton-X software package.[61] The MNDO/MRCI and amber MM computations in NAMD simulation are performed by MNDO99[62] and Tinker,[63] respectively. To perform QM/MM dynamics, a new interface is developed for the Newton-X package.

3. RESULTS

3.1. Stationary Points and MECI Optimization. From QM/MM optimization, one local minimum (Min) for the reactant, two transition states (TSs), and one intermediate (Int) are located for ground-state decomposition. The two TSs are referred as $TS_{O−O}$ and $TS_{C−C}$ as their imaginary vibrational modes correspond to O−O and C−C stretches, respectively. Three S_0/S_1 minimum energy conical intersections (MECIs) are located by the SF-BHHLYP/6-31G** in the gas phase and expressed as $CI_{O−O}$, $CI_{C−C}$, and $CI_{C−O}$. The relative energies and corresponding $\langle S^2 \rangle$ are summarized in Table S2. The key geometric parameters are summarized in Tables S3 and S4. The lowest adiabatic S_0, S_1, and S_2 PECs, key geometric parameters,

and Mlliken charge populations along the reaction path are plotted in Figure 1.

3.2. Adiabatic and Approximate Diabatic Potential Energy Curves. According to the natural orbital analyses from CAM-B3LYP (Figures S4 and S5) and the configurational coefficient from SF-BHHLYP calculations, some diabatic states are involved in the lowest singlet states as elucidated in Figure 2.
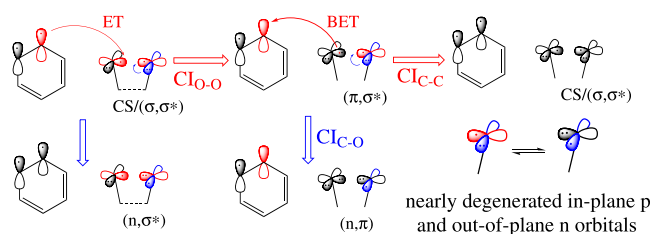
Figure 2. Elucidation of the diabatic states.

These diabatic PECs, which follow particular electronic configurations through conical intersections between two states of the same spin multiplicity, are plotted in Figure 3 diabatically from the adiabatic SF-DFT PECs by means of the diabatization proposed by Nakamura and Truhlar.[64] For the local Min of the RUB and DDO encounter complex, the S_0 state mainly consists of a typical closed-shell (CS) configuration. With the stretching of the O−O bond, the σ and σ^* orbitals of the peroxide bond are moving closer in energy and finally become two singular p orbitals on oxygen. After DDO dissociation, the S_0 state returns to a closed-shell configuration again. Therefore, we express the S_0 state as CS/(σ,σ^*). Meanwhile, the S_1 state changes from (π,π^*) to (π,σ^*) producing a typical CT process where the π and π^* are the delocalized π and π^* orbitals on the RUB fragment.
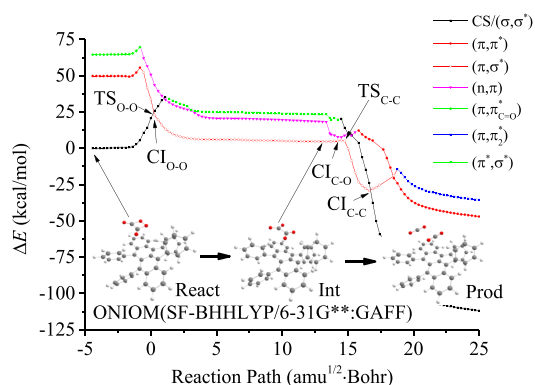
Figure 3. Approximate diabatic PECs calculated at the ONIOM(SF-BHHLYP/6-31G**:GAFF) level.

For the S_2 state, it is dominated by a $^1(\pi,\pi_{C=O}^*)$ configuration and gradually changes to a $^1(n,\pi^*)$ state with the elongation of the O−O bond, where the $\pi_{C=O}^*$ means the π^* orbital of C=O double bonds, while n is the nonbonding p orbital of O_4. The (n,π) state connects to a double transition from the nonbonding orbital of O_4 and the π orbital of RUB to the $O_3−O_4$ σ^* orbital. Therefore, we denoted the lowest three singlet states as CS/$^1(\sigma,\sigma^*)$, $^1(\pi,\pi^*)$/$^1(\pi,\sigma^*)$, and $^1(\pi,\pi_{C=O}^*)$/$^1(n,\pi)$.

3.3. Trajectory Surface Hopping Dynamics Simulation. For TSH simulation, the 211 trajectory stays in the reactant region all the time while 145 trajectories terminate abnormally due to the self-consistent filed unconvergence or energy unconservation. Finally, 244 trajectories from 600 initial samples successfully dissociate to two CO_2 fragments and are used in the following statistical analysis. The simulated branching ratios (Φ) for S_0-S_3 products are summarized in Table 1. The time

Table 1. Simulated Branching Ratios and Quantum Yields (Φ) with Standard Errors

state	N_{traj}	branching ratios	Φ_{CL}^{Sim}	Φ_{CL}^{∞}
S_0	113	0.463 ± 0.005		
S_1	70	0.287 ± 0.010	0.526	0.68
S_2	52	0.213 ± 0.015		
S_3	9	0.037 ± 0.107		

evolution of the key geometric parameters from a selected successful trajectory is shown in Figure 4A. The time evolution of the key geometric parameters, ensemble-averaged Mlliken charge population, and ensemble-averaged fractional occupations are plotted in Figure 4B−D, respectively. Two-dimensional distributions of the C−C and O−O bond lengths of $S_0 \leftrightarrow S_1$ hopping spots from TSH simulation are plotted in Figure 5A, while individual $S_0 \rightarrow S_1$ excitation and $S_1 \rightarrow S_0$ de-excitation distribution are plotted in Figure 5B,C. Based on the state population at the end of simulation, four typical trajectories that end on S_0-S_3 states are selected to show the energy conversations. Their time evolution data of the potential energy, kinetic energy, and total energy of the whole system and S_0-S_3 electronic energies of the QM region are plotted in Figures S6−S9, respectively.

4. DISCUSSION

4.1. ET-Catalyzed Stepwise Decomposition of DDO. *4.1.1. Stepwise Decomposition.* According to S_0 PEC and optimized geometric parameters (Figure 1A−C and Tables S3

and S4), the ET-catalyzed decomposition of DDO can be divided into two steps. First, the DDO decomposition is initiated by the $O_3−O_4$ bond dissociation, which proceeds through the first TS, $TS_{O−O}$ (the $O_3−O_4$ bond is 1.757 Å), to an intermediate, Int ($O_3−O_4$ is 2.537 Å). The $C_1−C_2$ bond remains intact (increases by only 0.025 Å) until the $O_3−O_4$ bond is completely broken. Then, the $C_1−C_2$ bond begins to dissociate, and two CO_2 molecules are finally produced after the reaction proceeds through the second TS, $TS_{C−C}$. Although variation of $O_3−C_1−C_2−O_4$ ($<\pm5°$) along the reaction path implies a planar reaction, the time evolution of $O_3−C_1−C_2−O_4$ for a selected trajectory from TSH simulation (Figure 4A) shows that the rotation around the $C_1−C_2$ bond is easy to occur after $O_3−O_4$ is completely broken down. Moreover, the decreases (increases) of the four $C_1−O_3$ and $C_2−O_4$ ($C_1−O_5$ and $C_2−O_6$) bond lengths are also asynchronous as shown in Figure 1C, indicating a different electronic population for the four oxygen atoms on DDO. The relative energies of the $TS_{O−O}$ and $TS_{C−C}$ are 18.5 (13.8 in the gas phase) and 9.9 (−0.5 in the gas phase) kcal/mol, respectively (Table S2), which are close to the experimental values (12.2 kcal/mol for 9,10-diphenylanthracene-catalyzed POCL),[65] indicate that the O−O cleavage is the rate-determination step for RUB-catalyzed DDO decomposition.

The TSH dynamics simulation also displays an asynchronous dissociation of O−O and C−C bonds. As shown by time evolution of the $C_1−C_2$ and $O_3−O_4$ distances (Figure 4B), only a small amount of trajectories dissociated within 50 fs. Most trajectories experience a periodic change of the $O_3−O_4$ distance (about 2.0−3.5 Å) before the $C_1−C_2$ dissociates. This indicates an unstable intermediate and a small barrier for C−C cleavage during the decomposition as revealed by the QM/MM optimization. Thus, both QM/MM optimization and TSH simulation reveal a stepwise chemiluminescence decomposition of DDO.

4.1.2. Singlet ET and BET. The configuration coefficients from SF-DFT calculations show that the S_0 states around the reactant (RUB + DDO) and the product (RUB + 2×CO_2) region are the closed-shell/$^1(\sigma,\sigma^*)$ state, while the S_0 state of Int is dominated by a $^1(\pi,\sigma^*)$ configuration with the RUB → DDO ET property. An RUB → DDO ET and DDO → RUB BET are hence expected during the decomposition. With the O−O elongation, a sudden single ET and DDO → RUB BET occur at IRC = −0.555 and 17.701 amu$^{1/2}$·Bohr, respectively, as shown by the Mlliken charge variation along the reaction path (Figure 1D). From $TS_{O−O}$ to $TS_{C−C}$, nearly one positive charge (0.9 |e|) and one negative charge (−0.9 |e|) are, respectively, populated on the RUB and DDO moieties in contrast to neutral RUB and DDO at the reactant region. As shown by the Mlliken charge variation (Figure 1D) and NO (Figure S5), the negative charge does not averagely populate on four oxygen atoms but focus on the O_4 atom, explaining the asynchronous stretches and shrinks of four C−O in Figure 1C. The time evolutions of average charge population from TSH simulation (Figure 4C) show that about 0.9 |e| and−0.9 |e| are, respectively, populated on the RUB and DDO moieties before 50 fs where most trajectories still stay at the Int region. A gradual BET from the DDO to RUB moiety is significant in 50−150 fs. Because most of the backward trajectories are trapped in the reactant region, the RUB → DDO ET process is not demonstrated. Nevertheless, the TSH simulation also confirmed the existence of cation/anion radical Int as well as the QM/MM optimization. Therefore, both the ET/BET process and the solvent-caged cation/anion radical pair (RUB$^+$ + DDO$^-$) described by the CIEEL mechanism are
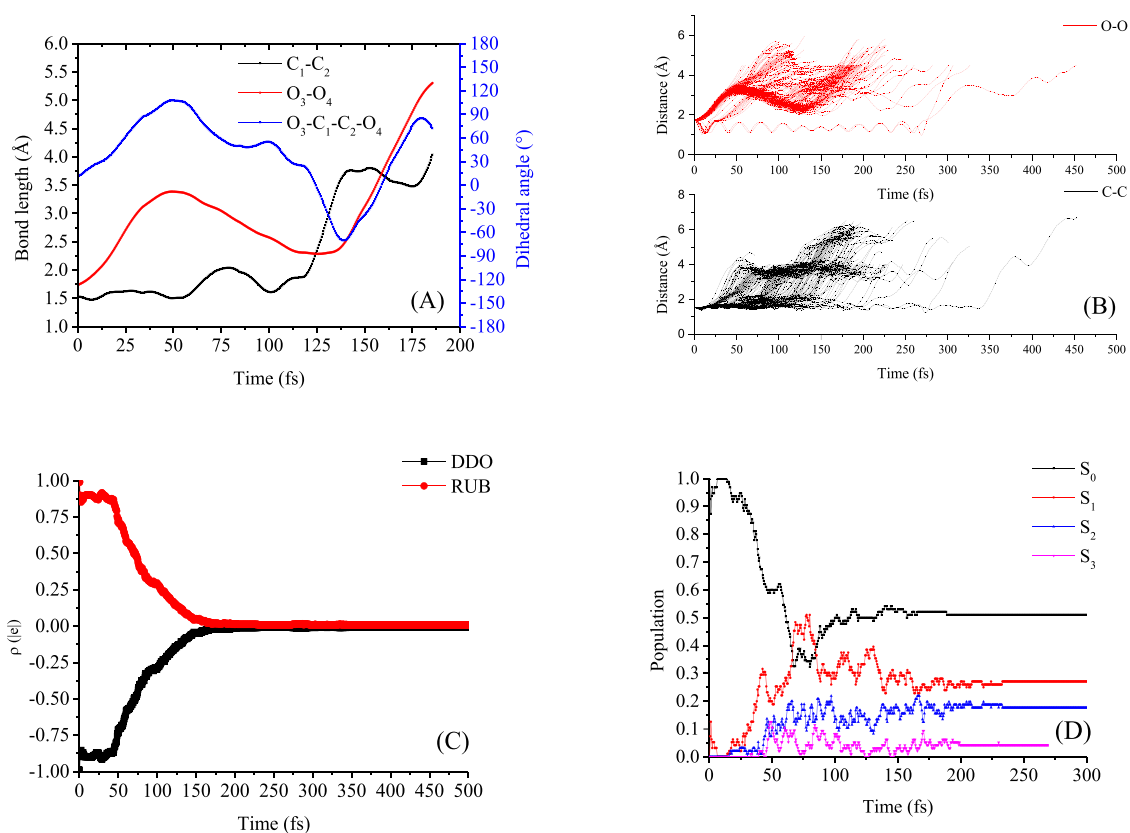
Figure 4. (A) Time evolution of key geometric parameters for a specifically selected trajectory, (B) for all successful trajectories, (C) the ensemble averaged Mlliken charge population on RUB and DDO moieties, and (D) the ensemble-averaged fractional occupation of S_0-S_3 state TSH simulation at the ONIOM(MNDO/MRCI:GAFF) level.

supported by current QM/MM calculations and TSH simulation.

**4.2. Three S_0/S_1 Conical Intersection-Controlled Singlet Chemiexcitation.** *4.2.1. CI_{O-O} and CI_{C-C}.* As the S_0 state of Int has different dominated configurations from the reactant and product, the diabatic $CS/(\sigma,\sigma^*)$ and (π,σ^*) states are expected to intersect with each other twice during the RUB-catalyzed DDO decomposition as shown by the approximate diabatic PECs in Figure 3. With the elongation of the O−O bond, the σ and σ^* orbitals of the peroxide bond get close with each other, not only increasing the energy of $CS/(\sigma,\sigma^*)$ but also lowering the (π,σ^*) state. At IRC = 0.278 amu$^{1/2}$·Bohr (the O−O distance is 1.780 A), the two diabatic states intersect with each other for the first time, switching the properties of S_0 and S_1 states. After that, the S_0 state retains the (π,σ^*) property with energy decreasing by about 16 kcal/mol. Then, the S_0 state energy does not change significantly until IRC = 14.502 amu$^{1/2}$·Bohr, where the C−C bond begins breaking. Finally, the S_0-(π,σ^*) PEC rapidly goes downhill again and intersects with the S_1-$CS/(\sigma,\sigma^*)$ state for the second time at IRC = 16.627 amu$^{1/2}$·Bohr, with the C−C bond partially dissociating.

Furthermore, the smallest energy gaps (3.2 and 5.4 kcal/mol, Figure 1A) between adiabatic S_0 and S_1 states at IRC = 0.278 and 16.627 amu$^{1/2}$·Bohr indicate that there could be two CIs between S_0 and S_1 PESs, respectively, at the O−O and C−C cleavage region. Both CIs are confirmed by the following MECI optimization at the SF-BHHLYP/6-31G** level in the gas phase. The displacements along the directions of DCV and GDV for CI_{O-O} are both close to the O−O stretch, while those for CI_{C-C} are close to C−C elongation (Figure S10 and gif

animation in the Supporting Information). This is why we express them as CI_{O-O} and CI_{C-C}, respectively. Thus, the two CIs, which come from the two crossings between diabatic $CS/(\sigma,\sigma^*)$ and (π,σ^*) states, are hence expected to provide high probability for the $S_0 \leftrightarrow S_1$ nonadiabatic transition. Similar CI_{O-O} and CI_{C-C} were also observed in ET-catalyzed CL of 1,2-dioxetane[20] and 1,2-dioxetanone.[24,26,30,66]

The hopping spot distributions from TSH simulation clearly demonstrate the $S_0 \leftrightarrow S_1$ nonadiabatic transitions around CI_{O-O} and CI_{C-C}. As shown in Figure 5A, the distribution of the $S_0 \leftrightarrow S_1$ hopping can be divided into three regions. In the first hopping region, the ranges of C−C/O−O distances (1.40−1.70/1.70−1.85 Å) are very close to the optimized C_1-C_2/O_3-O_4 (1.522/1.764 Å) bonds of CI_{O-O}, while the ranges of C−C/O−O distances in the second hopping region (1.70−2.3/2.00−3.25 Å) agree with the C_1-C_2/O_3-O_4 (2.016/2.796 Å) distances of CI_{C-C} (Table S3). In addition, the numbers of hopping spots in the CI_{O-O} (176) and CI_{C-C} (499) regions indicate that CI_{C-C} might provide more chances for the $S_0 \leftrightarrow S_1$ nonadiabatic transitions.

4.2.2. Third S_0/S_1 CI. Besides the hopping spots in CI_{O-O} (176) and CI_{C-C} (499), 163 hopping spots are distributed outside the above O−O and C−C bond breaking regions. Obviously, these nonignorable hopping spots whose C−C/O−O distances ranges in 1.40−1.70/2.00−3.10 Å can be attributed to neither CI_{O-O} nor CI_{C-C}. According to the approximate diabatic PECs in Figure 3, after the first intersection with the (π,σ^*) state, the S_1-$CS/(\sigma,\sigma^*)$ separates from the S_0-(π,σ^*) state and intersects with the diabatic S_2-(n,π) state at IRC = 1.112 amu$^{1/2}$·Bohr. The S_1 state hence changes its properties
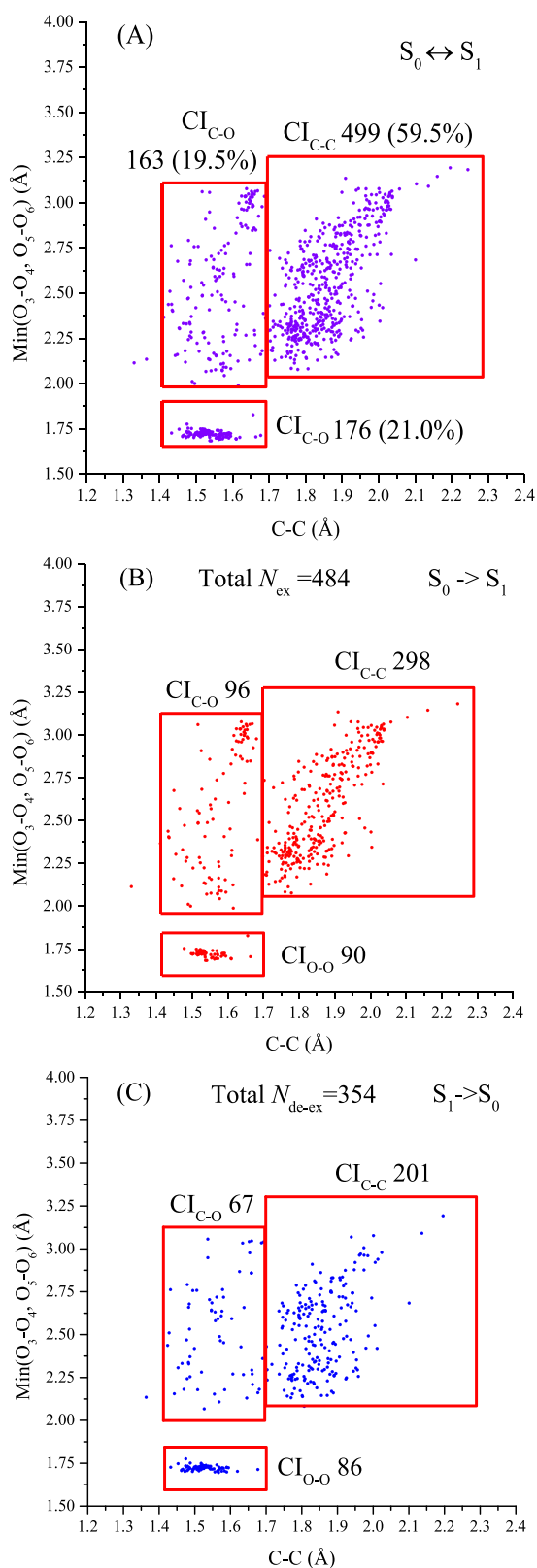
Figure 5. Two-dimensional hopping spot distributions along the O−O and C−C distances with the number and ratio of hopping spots in each CI region. (A) Scatter pattern for $S_0 \leftrightarrow S_1$ hopping, (B) scatter pattern for $S_0 \rightarrow S_1$ excitation, and (C) scatter pattern for $S_1 \rightarrow S_0$ de-excitation. For each hopping spot, the O−O distance is chosen from the minimum value in O_3-O_4 and O_5-O_6. The numbers of hopping spots are labeled for each CI region.

from $CS/(\sigma,\sigma^*)$ to (n,π) and retains the (n,π) configuration until IRC = 13.352 $amu^{1/2}$·Bohr. Then, the S_1-(n,π) PEC goes downhill and gets very close with the S_0-(π,σ^*) PEC until the C−C bond begins breaking at IRC = 14.502 $amu^{1/2}$·Bohr with the smallest S_0/S_1 energy gap of 2.3 kcal/mol (C−C/O−O distances are 1.526/2.543 Å). Then, the S_1-(n,π) PEC increases its energy and intersects with the $CS/(\sigma,\sigma^*)$ state for the second time at IRC = 15.013 $amu^{1/2}$·Bohr, changing the S_1 state to a $CS/(\sigma,\sigma^*)$ state.

Although the diabatic (π,σ^*) and (n,π) states do not seem to switch their energy levels at this region, the very small S_0/S_1 energy gap (2.3 kcal/mol) and the hopping spot distribution both imply the existence of the third S_0/S_1 CI at this region. What is more, the C−C/O−O bond lengths (1.526/2.543 Å) at this point are just in the third hopping spot region (1.40−1.70/2.00−3.10 Å) in Figure 5A. Indeed, when the O−O bond is completely broken, the in-plane p orbitals and out-of-plane n orbital on the same oxygen atom (O_4) can be degenerated at specific geometries, producing a new S_0/S_1 CIs as explained in Figure 2. Thus, we performed another MECI optimization and successfully located the third S_0/S_1 CI at the SF-BHHLY/6-31G** level in the gas phase; its displacements of GDV and DCV (Figure S10 and gif animation in the Supporting Information) are mainly contributed by the C_1-O_6 stretch. The newly discovered S_0/S_1 CI is hence expressed as CI_{C-O}. Since the C−O shrink occurs with the O−O/C−C dissociation, the CI_{C-O} can be expected to provide a considerable chance for the $S_0 \leftrightarrow S_1$ nonadiabatic transition as well as CI_{O-O} and CI_{C-C}, displayed by TSH simulation.

4.2.3. Quantum Yield of Singlet Chemiexcitation. According to the NAMD simulation by the Zhu−Nakamura trajectory surface hopping (TSH) algorithm, the final branching ratios of the ground- and excited-state products are computed using the Monte Carlo method with equal weight to all trajectories, i.e., branching ratios of state $i = N_i/N$, with the standard error using $\sigma_i = (N - N_i)/(N \times N_i)$, where N is the total number of successful trajectories and N_i is the number of successful trajectories terminated on state i. In the successful 244 trajectories, 70, 52, and 9 trajectories are terminated on S_1, S_2, and S_3 at the end of the simulation, and the branching ratios of S_1, S_2, and S_3 states are computed to be 0.287 ± 0.010, 0.213 ± 0.015, and 0.037 ± 0.107, respectively (Table 1). The final quantum yield of singlet-excited RUB (Φ_S) is hence estimated to be 0.537 ± 0.004. As the fluorescence quantum yield (Φ_f) of RUB is 0.98,[12,37] the simulated quantum yield of RUB-catalyzed DDO CL, Φ_{CL}, is about 52.6%, which is very close to the experimental observations (ca. 0.6, $\Phi_{CL}^{\infty} = 0.68$).[37] The high efficiency of singlet chemiexcitation in line with the experimental values confirms the ET-catalyzed DDO decomposition as the chemical origin of POCL.

4.3. The Role of Three S_0/S_1 CIs in High-Efficiency Singlet Chemiexcitation. *4.3.1. Topology of Three S_0/S_1 CIs.* The CI_{O-O} and CI_{C-C}, which originate from two crossings between diabatic $CS/(\sigma,\sigma^*)$ and (π,σ^*) states, are found and characterized in many other intramolecular ET-catalyzed decomposition of cyclic peroxides before,[18,20,26,27,30,31,66,67] while the CI_{C-O} has been discovered and characterized for the first time. To elucidate the role of the three CIs, the two-dimensional PESs were scanned around the three S_0/S_1 CIs along the GDV and DCV directions as shown in Figure 6 and Figure S11. For all the three CIs, the corresponding vectors of GDV and DCV have a large norm in one direction and a small norm in the other direction. As the process is diabatic, the
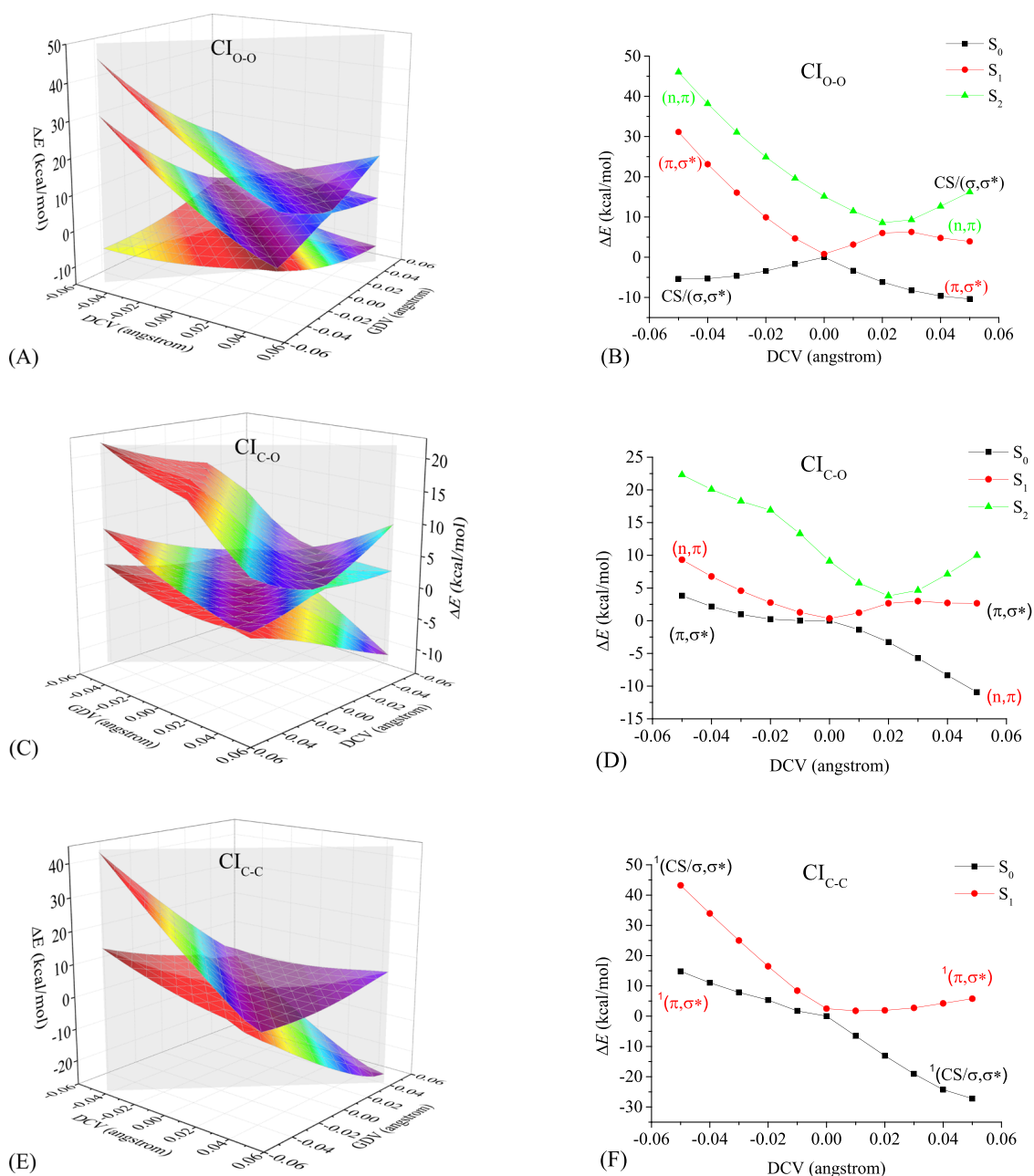
Figure 6. Two-dimensional S_0 and S_1 PESs (kcal/mol) and the corresponding cross sections in terms of the DCV and GDV directions (Å) at the SF-TDDFT/6-31G** level.

branching space (BS) can be seen as one-dimensional and the intersection seam as a 3N-7-dimensional vector space, instead of the normal two-dimensional BS and 3N-8 dimensional intersection space. Thus, the crossing between the S_0 and S_1 PESs looks like an intersection seam but not a normal double cone[56,68] as shown in Figure 6A,C,E and Figure S11. Therefore, during the O−O/C−C stretch and C−O shrink in DDO decomposition, all the three S_0/S_1 CIs could provide a widely extended channel to diabatically access the S_1 from the S_0 state when the molecules have enough velocity (kinetic energy) along the direction of DCV or GDV. Indeed, in current TSH simulation, a total of 484 $S_0 \rightarrow S_1$ excitations occur in 244 successful trajectories, which means that two $S_0 \rightarrow S_1$ excitations on average could occur in a trajectory evolution.

Moreover, the CI_{O-O} is very close to the adiabatic TS_{O-O}, so no additional kinetic energies could provide for the O−O

stretch. For CI_{C-O}, about 17.3 kcal/mol ($E_{IRC\ =\ 0.278} - E_{IRC\ =\ 14.502}$ on S_0 PEC in Figure 1A) potential energy change can be provided for the following O−O stretch and four C−O stretches or shrinks. Thus, only a few kcal/mol kinetic energies might be expected to be added on each C−O stretch or shrink mode for CI_{C-O}. In contrast to above two CIs, the S_0 PEC rapidly goes downhill along the C−C elongation; the large potential energy change, 33.1 kcal/mol ($E_{IRC\ =\ 14.502} - E_{IRC\ =\ 16.627}$ on S_0 PEC in Figure 1A), could provide considerable kinetic energy and velocity along the C−C stretch. This explains why the CI_{C-C} provides the most $S_0 \rightarrow S_1$ excitation (61.6%) in TSH simulation. In contrast, the hopping spots of $S_0 \rightarrow S_1$ excitation at CI_{O-O} and CI_{C-O} are only 19.8 and 18.6%, respectively.

4.3.2. Net $S_0 \rightarrow S_1$ Chemiexcitation. According to the excitation (Figure 5B) and de-excitation (Figure 5C) distribu-
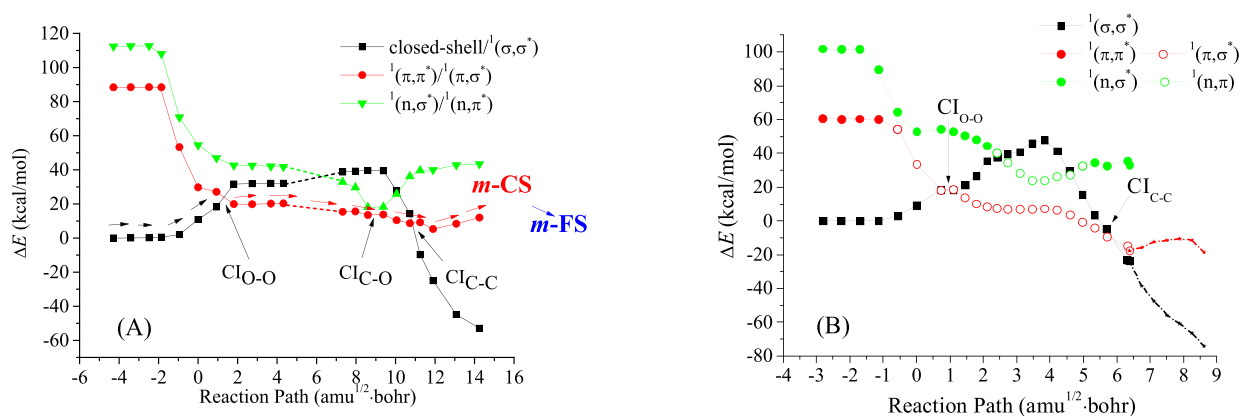
Figure 7. Diabatic PECs calculated by at the MS-CASPT2//CAM-B3LYP level for (A) *m*-AMPPD, reprinted with permission from ref 20. Copyright 2013 American Chemical Society. (B) The diabatic PECs calculated at the CASPT2//CAM-B3LYP level for firefly dioxetanone, reprinted with permission from ref 30.

tions, the number of excitation ($S_0 \rightarrow S_1$) is obviously more than that of de-excitation ($S_1 \rightarrow S_0$) at CI_{C-O} and CI_{C-C} (N_{ex} : $N_{de-ex} \approx 3 : 2$) while the excitation and de-excitation are nearly the same at CI_{O-O} ($N_{ex} : N_{de-ex} \approx 1 : 1$). This indicates that the CI_{C-O} and CI_{C-C} contributed most for the net $S_0 \rightarrow S_1$ chemiexcitation. As shown by the PES topology (Figure 6), both CI_{C-O} and CI_{C-C} are sloped CIs (tilted) while the CI_{O-O} is close to a vertical (nontilted) one. A similar sloped conical intersection with one-dimensional branching spaces and 3N-7 dimensional intersection seam was observed and characterized for firefly dioxetanone by Chung et al.[24] For CI_{C-O} and CI_{C-C}, the tilted "double cones" means that they could transform to the final excited products via a small energy barrier process for CI_{C-O} (about 2.3 kcal/mol in Figure 6D) or a barrierless process for CI_{C-C} (Figure 6E), providing a high net $S_0 \rightarrow S_1$ chemiexcitation. In contrast, the molecules excited at CI_{O-O} might have to overcome a higher energy barrier on the S_1 surface (6.9 kcal/mol in Figure 6B) to complete the following excited-state reaction. Thus, most of the molecules excited at CI_{O-O} have to return to the S_0 state via the same path. The net $S_0 \rightarrow S_1$ chemiexcitation for CI_{O-O} is hence close to zero. This is also reflected by the ensemble-averaged fractional occupation of the S_1 state (Figure 4D) in which the S_1 population decreases from the peak (at 80 fs) 0.51 to final 0.287.

4.3.3. Universality of CI_{C-O}. Besides in DDO, the CI_{O-O} and CI_{C-C} have been discovered in many other high-efficiency 1,2-dioxetane and 1,2-dioxetanone systems.[20,26,27,30,31,66,69,70] Similarly, the CI_{C-O} might also be widespread in various ET-catalyzed CL of cyclic peroxides. In fact, the very close (π,σ^*) and (n,π) PECs have been observed in our previous work on chemiluminescence decomposition of *m*-AMPPD as shown in Figure 7A. The smallest S_0/S_1 energy gap is 4.5 kcal/mol with C−C/O−O bonds of 1.602/2.450 Å at the CASPT2//CAM-B3LYP level for *m*-AMPPD. However, because the energy level exchange between diabatic (π,σ^*) and (n,π) states was not observed and NAMD simulation was not performed in that work, the existence and possibility of the CI_{C-O} were ignored by the authors. Obviously, the CI_{C-O}, which originates from the nearly degenerated n and p orbitals on the same oxygen, can also be expected in *m*-AMPPD CL. In fact, these degenerated p orbitals of oxygen can allow the intersections between (σ,σ^*) and (n,σ^*) states in the uncatalyzed decomposition of 1,2-dioxetanes[13] and 1,2-dioxetanones,[15] inducing a wide range of nearly degenerated S_0 and S_1 PESs. Thus, the CI_{C-O} structure

was universally expected to exist in ET-catalyzed decomposition of cyclic peroxides at specific geometries. However, not all ET-catalyzed chemiluminescence decomposition could be actually observed to have very close (π,σ^*) and (n,π) PECs along the S_0 reaction path. The intramolecular ET-catalyzed 1,2-dioxetanone like firefly chemiluminescence has a more than 16.6 kcal/mol energy gap between (π,σ^*) and (n,π) states along the S_0 PEC as shown in Figure 7B. According to the geometries and electronic properties of CI_{C-O}, we could infer that the O−O bond should be completely broken down and the C−C bond is still attached for a CI_{C-O}. Otherwise, the in-plane p orbital of oxygen will couple with the p orbitals on the other oxygen or carbon atom nearby, increasing the energy gap between (π,σ^*) and (n,π) states. Thus, a biradical intermediates with one singularly occupied in-plane p orbital of oxygen might be required to encounter a CI_{C-O} along the reaction path. This could explain why we only observed the very closed (π,σ) and (n,π) PECs in the ET-catalyzed decomposition of 1,2-dioxetane (*m*-AMPPD) and DDO. For the asynchronous one-step ET-catalyzed decomposition like firefly dioxetanone, the singularly occupied in-plane p orbital is immediately coupled with the C−C bond after the O−O bond completely breaks down, so CI_{C-O} might be difficult to encounter along the reaction path.

5. CONCLUSIONS

In this work, we have performed the first QM/MM optimization and QM/MM NAMD simulation on the rubrene-catalyzed decomposition of 1,2-dioxetanedione, which is considered as the key process for high-efficiency peroxyoxalate chemilumines-cence. The stepwise decomposition via a cation/anion radical pair assumed by the intermolecular CIEEL is confirmed by both QM/MM calculations and NAMD simulation. The simulated high quantum yield of chemiluminescence ($\Phi_{CL} = 0.526$) agrees with the experimental values ($\Phi_{CL}^{\infty} = 0.68$) supporting 1,2-dioxetanedione as the key intermediate for POCL. Three S_0/S_1 conical intersections, CI_{O-O}, CI_{C-C}, and CI_{C-O}, are confirmed by MECI optimization and TSH simulation. All of them have 3N-7 dimensional intersection spaces, and the one-dimensional branching spaces, corresponding to O−O, C−C, and C−O stretches, could provide a widely extended channel to the $S_0 \rightarrow S_1$ nonadiabatic excitation. The three types of S_0/S_1 CIs are not a special case in ET-catalyzed DDO CL but can be universal in many other four-membered cyclic peroxides including 1,2-dioxetane and 1,2-dioxetanone derivatives. They play different

roles in the high-efficiency singlet chemiexcitation in ET-catalyzed CL of 1,2-dioxetanedione and should be the true origin of high-efficiency singlet CL. The present theoretical investigation uncovers the detailed mechanism of the rubrene-catalyzed decomposition of 1,2-dioxetanedione and elucidates the different roles played by the S_0/S_1 CIs for the first time. We believe that this work does not only provide a further understanding and a stepping stone for future studies on the high-efficiency ET-catalyzed CL but also can inspire experimental designs of new high-efficiency singlet chemiluminescent systems and reactions.

■ ASSOCIATED CONTENT

ⓢ Supporting Information

The Supporting Information is available free of charge at https://pubs.acs.org/doi/10.1021/acs.jctc.1c00356.

(Chart S1) The chemical structures of 1,2-dioxetane, 1,2-dioxetanone, 1,2-dioxetanedione, bis(2,4,6-trichlorophenyl) oxalate, and rubrene; (Figure S1) the PMF along the distance between the geometric centers of RUB and DDO fragments obtained by umbrella samplings with the general Amber force field in gas and ethyl acetate; (Figure S2) the comparison of optimized bond lengths, bond angles, and dihedral angles for the Min, Int, TS_{O-O}, and TS_{C-C} by the ONIOM with different basis sets; (Figure S3) the adiabatic S_0, S_1, and S_2 PECs by semiempirical MRCI methods along the reaction path by ONIOM(CAM-B3LYP/6-31G**:GAFF); (Figure S4) the important molecular orbitals for Min; (Figure S5) the important natural orbitals and the occupation numbers of the S_0 state for TS_{O-O}, Int, and TS_{C-C}; time evolution of the potential, kinetic, and total energies of the whole system and the adiabatic S_0, S_1, S_2, and S_3 potential energies of the QM region for a selective trajectory, which ends on the S_0 state (Figure S6), the S_1 state (Figure S7), the S_2 state (Figure S8), and the S_3 state (Figure S9); (Figure S10) the derivative coupling vector (DCV) and gradient difference vector (DCV) of the CI_{O-O}, CI_{C-C}, and CI_{C-O}; (Figure S11) two-dimensional S_0 and S_1 PESs (kcal/mol) for CI_{O-O}, CI_{C-O}, and CI_{C-C} at the SFTDDFT/6-31G** level; (Table S1) the serial number of the internal coordinates on the DDO moiety; (Table S2) the QM and QM/MM relative energies and $<S^2>$ of optimized Min, TS, and Int in EAC and MECI in the gas phase; (Table S3) the key geometric parameters of optimized Min, TS, and, Int by ONIOM(SFBHHLYP/6-31G**:GAFF) in EAC and MECI by SF-BHHLYP/6-31G** in the gas phase; (Table S4) the key geometric parameters of optimized Min, TS, and Int by ONIOM(CAMB3LYP/6-31G**:GAFF) in EAC; the optimized Cartesian coordinates at the SF-BHHLYP/6-31G** level (PDF)

Compressed displacement movies of DCV and GDV for CI_{O-O}, CI_{C-O}, and CI_{C-C} (ZIP)

Compressed PDB files for the optimized key stationary points (ZIP)

■ AUTHOR INFORMATION

Corresponding Authors

Ling Yue − *Key Laboratory for Non-Equilibrium Synthesis and Modulation of Condensed Matter, Ministry of Education, School of Chemistry, Xi'an Jiaotong University, Xi'an, Shaanxi 710049, China;* ⓞ orcid.org/0000-0001-5060-9947; Email: heartstar@mail.xjtu.edu.cn

Ya-Jun Liu − *Center for Advanced Materials Research, Advanced Institute of Natural Sciences, Beijing Normal University, Zhuhai 519087, China; Key Laboratory of Theoretical and Computational Photochemistry, Ministry of Education, College of Chemistry, Beijing Normal University, Beijing 100875, China;* ⓞ orcid.org/0000-0001-8761-5339; Email: yajun.liu@bnu.edu.cn

Complete contact information is available at:
https://pubs.acs.org/10.1021/acs.jctc.1c00356

Notes

The authors declare no competing financial interest.

■ ACKNOWLEDGMENTS

■ REFERENCES

(1) Su, Y.; Chen, H.; Wang, Z.; Lv, Y. Recent Advances in Chemiluminescence. *Appl. Spectrosc. Rev.* **2007**, *42*, 139−176.

(2) Strehler, B. L. Bioluminescence Assay: Principles and Practice. In *Methods Biochem. Anal.*; John Wiley & Sons, Inc.: 2006; pp 99−181.

(3) Romanyuk, A. V.; Grozdova, I. D.; Ezhov, A. A.; Melik-Nubarov, N. S. Peroxyoxalate Chemiluminescent Reaction as a Tool for Elimination of Tumour Cells Under Oxidative Stress. *Sci. Rep.* **2017**, *7*, 3410.

(4) McCapra, F. The chemiluminescence of organic compounds. *Q. Rev., Chem. Soc.* **1966**, *20*, 485−510.

(5) White, E. H.; Roswell, D. F. Chemiluminescence of organic hydrazides. *Acc. Chem. Res.* **1970**, *3*, 54−62.

(6) Matsumoto, M. Advanced chemistry of dioxetane-based chemiluminescent substrates originating from bioluminescence. *J. Photochem. Photobiol. C: Photochem. Rev.* **2004**, *5*, 27−53.

(7) Adam, W.; Kazakov, D. V.; Kazakov, V. P. Singlet-Oxygen Chemiluminescence in Peroxide Reactions. *Chem. Rev.* **2005**, *105*, 3371−3387.

(8) Koo, J.-Y.; Schuster, G. B. Chemically initiated electron exchange luminescence. A new chemiluminescent reaction path for organic peroxides. *J. Am. Chem. Soc.* **1977**, *99*, 6107−6109.

(9) Adam, W.; Baader, W. J. Effects of methylation on the thermal stability and chemiluminescence properties of 1,2-dioxetanes. *J. Am. Chem. Soc.* **1985**, *107*, 410−416.

(10) Adam, W.; Bronstein, I.; Trofimov, A. V.; Vasil'ev, R. F. Solvent-Cage Effect (Viscosity Dependence) as a Diagnostic Probe for the Mechanism of the Intramolecular Chemically Initiated Electron-Exchange Luminescence (CIEEL) Triggered from a Spiroadamantyl-Substituted Dioxetane. *J. Am. Chem. Soc.* **1999**, *121*, 958−961.

(11) Bartoloni, F. H.; Oliveira, M. A. d.; Augusto, F. A.; Ciscato, L. F. M. L.; Bastos, E. L.; Baader, W. J. Synthesis of unstable cyclic peroxides for chemiluminescence studies. *J. Braz. Chem. Soc.* **2012**, *23*, 2093−2103.

(12) Augusto, F. A.; de Souza, G. A.; de Souza Júnior, S. P.; Khalid, M.; Baader, W. J. Efficiency of Electron Transfer Initiated Chemiluminescence. *Photochem. Photobiol.* **2013**, *89*, 1299−1317.

(13) De Vico, L.; Liu, Y.-J.; Krogh, J. W.; Lindh, R. Chemiluminescence of 1,2-Dioxetane. Reaction Mechanism Uncovered. *J. Phys. Chem. A* **2007**, *111*, 8013−8019.

(14) Bos, R.; Tonkin, S. A.; Hanson, G. R.; Hindson, C. M.; Lim, K. F.; Barnett, N. W. In Search of a Chemiluminescence 1,4-Dioxy Biradical. *J. Am. Chem. Soc.* **2009**, *131*, 2770−2771.

(15) Liu, F.; Liu, Y.; De Vico, L.; Lindh, R. Theoretical Study of the Chemiluminescent Decomposition of Dioxetanone. *J. Am. Chem. Soc.* **2009**, *131*, 6181−6188.

(16) Almeida de Oliveira, M.; Bartoloni, F. H.; Augusto, F. A.; Ciscato, L. F. M. L.; Bastos, E. L.; Baader, W. J. Revision of Singlet Quantum Yields in the Catalyzed Decomposition of Cyclic Peroxides. *J. Org. Chem.* **2012**, *77*, 10537−10544.

(17) de Jong, W. A.; Lischka, H.; Windus, T. L.; Hase, W. L. Direct dynamics simulation of dioxetane formation and decomposition via the singlet ·O−O−CH2−CH2· biradical: Non-RRKM dynamics. *J. Chem. Phys.* **2012**, *137*, No. 044305.

(18) Yue, L.; Roca-Sanjuán, D.; Lindh, R.; Ferré, N.; Liu, Y.-J. Can the Closed-Shell DFT Methods Describe the Thermolysis of 1,2-Dioxetanone? *J. Chem. Theory Comput.* **2012**, *8*, 4359−4363.

(19) Farahani, P.; Roca-Sanjuán, D.; Zapata, F.; Lindh, R. Revisiting the Nonadiabatic Process in 1,2-Dioxetane. *J. Chem. Theory Comput.* **2013**, *9*, 5404−5411.

(20) Yue, L.; Liu, Y.-J. Mechanism of AMPPD Chemiluminescence in a Different Voice. *J. Chem. Theory Comput.* **2013**, *9*, 2300−2312.

(21) Vacher, M.; Fdez. Galván, I.; Ding, B.-W.; Schramm, S.; Berraud-Pache, R.; Naumov, P.; Ferré, N.; Liu, Y.-J.; Navizet, I.; Roca-Sanjuán, D.; Baader, W. J.; Lindh, R. Chemi- and Bioluminescence of Cyclic Peroxides. *Chem. Rev.* **2018**, *118*, 6927−6974.

(22) Takano, Y.; Tsunesada, T.; Isobe, H.; Yoshioka, Y.; Yamaguchi, K.; Saito, I. Theoretical Studies of Decomposition Reactions of Dioxetane, Dioxetanone, and Related Species. CT Induced Luminescence Mechanism Revisited. *Bull. Chem. Soc. Jpn.* **1999**, *72*, 213−225.

(23) Isobe, H.; Takano, Y.; Okumura, M.; Kuramitsu, S.; Yamaguchi, K. Mechanistic Insights in Charge-Transfer-Induced Luminescence of 1,2-Dioxetanones with a Substituent of Low Oxidation Potential. *J. Am. Chem. Soc.* **2005**, *127*, 8667−8679.

(24) Chung, L. W.; Hayashi, S.; Lundberg, M.; Nakatsu, T.; Kato, H.; Morokuma, K. Mechanism of Efficient Firefly Bioluminescence via Adiabatic Transition State and Seam of Sloped Conical Intersection. *J. Am. Chem. Soc.* **2008**, *130*, 12880−12881.

(25) Liu, F.; Liu, Y.; Vico, L. D.; Lindh, R. A CASSCF/CASPT2 approach to the decomposition of thiazole-substituted dioxetanone: Substitution effects and charge-transfer induced electron excitation. *Chem. Phys. Lett.* **2009**, *484*, 69−75.

(26) Ding, B.-W.; Liu, Y.-J. Bioluminescence of Firefly Squid via Mechanism of Single Electron-Transfer Oxygenation and Charge-Transfer-Induced Luminescence. *J. Am. Chem. Soc.* **2017**, *139*, 1106−1119.

(27) Yue, L. QM/MM Investigations on the Bioluminescent Decomposition of Coelenterazine Dioxetanone in Obelin. *Chem. Res. Chin. Univ.* **2018**, *34*, 758−766.

(28) Horn, K. A.; Schuster, G. B. Electronic excitation energy partitioning in dissymmetric dioxetane thermolyses. The absolute chemiluminescence yields and triplet to singlet excited state ratios for 3-acetyl-4,4-dimethyl-1,2-dioxetane. *J. Am. Chem. Soc.* **1978**, *100*, 6649−6656.

(29) McCapra, F. Alternative mechanism for dioxetan decomposition. *J. Chem. Soc., Chem. Commun.* **1977**, 946−948.

(30) Yue, L.; Liu, Y.-J.; Fang, W.-H. Mechanistic Insight into the Chemiluminescent Decomposition of Firefly Dioxetanone. *J. Am. Chem. Soc.* **2012**, *134*, 11632−11639.

(31) Yue, L.; Liu, Y.-J. Two Conical Intersections Control Luminol Chemiluminescence. *J. Chem. Theory Comput.* **2019**, *15*, 1798−1805.

(32) Yue, L.; Liu, Y.-T. Mechanistic Insight into pH-Dependent Luminol Chemiluminescence in Aqueous Solution. *J. Phys. Chem. B* **2020**, *124*, 7682−7693.

(33) Wang, M.-Y.; Liu, Y.-J. Chemistry in Fungal Bioluminescence: A Theoretical Study from Luciferin to Light Emission. *J. Org. Chem.* **2021**, *86*, 1874−1881.

(34) Pinto da Silva, L.; Esteves da Silva, J. C. G. Mechanistic study of the unimolecular decomposition of 1,2-dioxetanedione. *J. Phys. Org. Chem.* **2013**, *26*, 659−663.

(35) Farahani, P.; Baader, W. J. Unimolecular Decomposition Mechanism of 1,2-Dioxetanedione: Concerted or Biradical? That is the Question! *J. Phys. Chem. A* **2017**, *121*, 1189−1194.

(36) Chandross, E. A. A new chemiluminescent system. *Tetrahedron Lett.* **1963**, *4*, 761−765.

(37) Stevani, C. V.; Silva, S. M.; Baader, W. J. Studies on the Mechanism of the Excitation Step in Peroxyoxalate Chemiluminescence. *Eur. J. Org. Chem.* **2000**, *2000*, 4037−4046.

(38) Catherall, C. L. R.; Palmer, T. F.; Cundall, R. B. Determination of absolute chemiluminescence quantum yields for reactions of bis-(pentachlorophenyl) oxalate, hydrogen peroxide and fluorescent compounds. *J. Biolumin. Chemilumin.* **1989**, *3*, 147−154.

(39) Augusto, F. A.; Francés-Monerris, A.; Fdez Galván, I.; Roca-Sanjuán, D.; Bastos, E. L.; Baader, W. J.; Lindh, R. Mechanism of activated chemiluminescence of cyclic peroxides: 1,2-dioxetanes and 1,2-dioxetanones. *Phys. Chem. Chem. Phys.* **2017**, *19*, 3955−3962.

(40) Johannes, K. Umbrella sampling. *Wiley Interdiscip. Rev.: Comput. Mol. Sci.* **2011**, *1*, 932−942.

(41) Grossfield, A. "WHAM: the weighted histogram analysis method", http://membrane.urmc.rochester.edu/content/wham, version 2.0.9.

(42) Case, D. A.; Babin, V.; Berryman, J. T.; Betz, R. M.; Cai, Q.; Cerutti, D. S.; T.E. Cheatham, I.; Darden, T. A.; Duke, R. E.; Gohlke, H.; Goetz, A. W.; Gusarov, S.; Homeyer, N.; Janowski, P.; Kaus, J.; Kolossváry, I.; Kovalenko, A.; Lee, T. S.; LeGrand, S.; Luchko, T.; Luo, R.; Madej, B.; Merz, K. M.; Paesani, F.; Roe, D. R.; Roitberg, A.; Sagui, C.; Salomon-Ferrer, R.; Seabra, G.; Simmerling, C. L.; Smith, W.; Swails, J.; Walker, R. C.; Wang, J.; Wolf, R. M.; Wu, X.; Kollman, P. A. *Amber 14*, University of California: San Francisco, 2014.

(43) Wang, J.; Wolf, R. M.; Caldwell, J. W.; Kollman, P. A.; Case, D. A. Development and testing of a general amber force field. *J. Comput. Chem.* **2004**, *25*, 1157−1174.

(44) Shao, Y.; Head-Gordon, M.; Krylov, A. I. The spin−flip approach within time-dependent density functional theory: Theory and applications to diradicals. *J. Chem. Phys.* **2003**, *118*, 4807−4818.

(45) Maeda, S.; Ohno, K.; Morokuma, K. Updated Branching Plane for Finding Conical Intersections without Coupling Derivative Vectors. *J. Chem. Theory Comput.* **2010**, *6*, 1538−1545.

(46) Yanai, T.; Tew, D. P.; Handy, N. C. A new hybrid exchange−correlation functional using the Coulomb-attenuating method (CAM-B3LYP). *Chem. Phys. Lett.* **2004**, *393*, 51−57.

(47) Schmidt, M. W.; Baldridge, K. K.; Boatz, J. A.; Elbert, S. T.; Gordon, M. S.; Jensen, J. H.; Koseki, S.; Matsunaga, N.; Nguyen, K. A.; Su, S.; Windus, T. L.; Dupuis, M.; Montgomery, J. A. General atomic and molecular electronic structure system. *J. Comput. Chem.* **1993**, *14*, 1347−1363.

(48) Frisch, M. J.; Trucks, G. W.; Schlegel, H. B.; Scuseria, G. E.; Robb, M. A.; Cheeseman, J. R.; Scalmani, G.; Barone, V.; Petersson, G. A.; Nakatsuji, H.; Li, X.; Caricato, M.; Marenich, A. V.; Bloino, J.; Janesko, B. G.; Gomperts, R.; Mennucci, B.; Hratchian, H. P.; Ortiz, J. V.; Izmaylov, A. F.; Sonnenberg, J. L.; Williams; Ding, F.; Lipparini, F.; Egidi, F.; Goings, J.; Peng, B.; Petrone, A.; Henderson, T.; Ranasinghe, D.; Zakrzewski, V. G.; Gao, J.; Rega, N.; Zheng, G.; Liang, W.; Hada, M.; Ehara, M.; Toyota, K.; Fukuda, R.; Hasegawa, J.; Ishida, M.; Nakajima, T.; Honda, Y.; Kitao, O.; Nakai, H.; Vreven, T.; Throssell, K.; Montgomery, J. A., Jr.; Peralta, J. E.; Ogliaro, F.; Bearpark, M. J.; Heyd, J.J.; Brothers, E. N.; Kudin, K. N.; Staroverov, V. N.; Keith, T. A.; Kobayashi, R.; Normand, J.; Raghavachari, K.; Rendell, A. P.; Burant, J. C.; Iyengar, S. S.; Tomasi, J.; Cossi, M.; Millam, J. M.; Klene, M.; Adamo, C.; Cammi, R.; Ochterski, J. W.; Martin, R. L.; Morokuma, K.; Farkas, O.; Foresman, J. B.; Fox, D. J. *Gaussian 16 Rev. A.03*; Gaussian, inc.: Wallingford, CT, 2016.

(49) Shao, Y.; Gan, Z.; Epifanovsky, E.; Gilbert, A. T. B.; Wormit, M.; Kussmann, J.; Lange, A. W.; Behn, A.; Deng, J.; Feng, X.; Ghosh, D.; Goldey, M.; Horn, P. R.; Jacobson, L. D.; Kaliman, I.; Khaliullin, R. Z.; Kuś, T.; Landau, A.; Liu, J.; Proynov, E. I.; Rhee, Y. M.; Richard, R. M.; Rohrdanz, M. A.; Steele, R. P.; Sundstrom, E. J.; Woodcock, H. L.; Zimmerman, P. M.; Zuev, D.; Albrecht, B.; Alguire, E.; Austin, B.; Beran, G. J. O.; Bernard, Y. A.; Berquist, E.; Brandhorst, K.; Bravaya, K. B.; Brown, S. T.; Casanova, D.; Chang, C.-M.; Chen, Y.; Chien, S. H.;

Closser, K. D.; Crittenden, D. L.; Diedenhofen, M.; DiStasio, R. A.; Do, H.; Dutoi, A. D.; Edgar, R. G.; Fatehi, S.; Fusti-Molnar, L.; Ghysels, A.; Golubeva-Zadorozhnaya, A.; Gomes, J.; Hanson-Heine, M. W. D.; Harbach, P. H. P.; Hauser, A. W.; Hohenstein, E. G.; Holden, Z. C.; Jagau, T.-C.; Ji, H.; Kaduk, B.; Khistyaev, K.; Kim, J.; Kim, J.; King, R. A.; Klunzinger, P.; Kosenkov, D.; Kowalczyk, T.; Krauter, C. M.; Lao, K. U.; Laurent, A. D.; Lawler, K. V.; Levchenko, S. V.; Lin, C. Y.; Liu, F.; Livshits, E.; Lochan, R. C.; Luenser, A.; Manohar, P.; Manzer, S. F.; Mao, S.-P.; Mardirossian, N.; Marenich, A. V.; Maurer, S. A.; Mayhall, N. J.; Neuscamman, E.; Oana, C. M.; Olivares-Amaya, R.; O'Neill, D. P.; Parkhill, J. A.; Perrine, T. M.; Peverati, R.; Prociuk, A.; Rehn, D. R.; Rosta, E.; Russ, N. J.; Sharada, S. M.; Sharma, S.; Small, D. W.; Sodt, A.; Stein, T.; Stück, D.; Su, Y.-C.; Thom, A. J. W.; Tsuchimochi, T.; Vanovschi, V.; Vogt, L.; Vydrov, O.; Wang, T.; Watson, M. A.; Wenzel, J.; White, A.; Williams, C. F.; Yang, J.; Yeganeh, S.; Yost, S. R.; You, Z.-Q.; Zhang, I. Y.; Zhang, X.; Zhao, Y.; Brooks, B. R.; Chan, G. K. L.; Chipman, D. M.; Cramer, C. J.; Goddard, W. A.; Gordon, M. S.; Hehre, W. J.; Klamt, A.; Schaefer, H. F.; Schmidt, M. W.; Sherrill, C. D.; Truhlar, D. G.; Warshel, A.; Xu, X.; Aspuru-Guzik, A.; Baer, R.; Bell, A. T.; Besley, N. A.; Chai, J.-D.; Dreuw, A.; Dunietz, B. D.; Furlani, T. R.; Gwaltney, S. R.; Hsu, C.-P.; Jung, Y.; Kong, J.; Lambrecht, D. S.; Liang, W.; Ochsenfeld, C.; Rassolov, V. A.; Slipchenko, L. V.; Subotnik, J. E.; van Voorhis, T.; Herbert, J. M.; Krylov, A. I.; Gill, P. M. W.; Head-Gordon, M. Advances in molecular quantum chemistry contained in the Q-Chem 4 program package. *Mol. Phys.* **2015**, *113*, 184−215.

(50) Tully, J. C. Mixed quantum-classical dynamics. *Faraday Discuss.* **1998**, *110*, 407−419.

(51) Kapral, R.; Ciccotti, G. Mixed quantum-classical dynamics. *J. Chem. Phys.* **1999**, *110*, 8919−8929.

(52) Yu, L.; Xu, C.; Lei, Y.; Zhu, C.; Wen, Z. Trajectory-based nonadiabatic molecular dynamics without calculating nonadiabatic coupling in the avoided crossing case: *trans* ↔ *cis* photoisomerization in azobenzene. *Phys. Chem. Chem. Phys.* **2014**, *16*, 25883−25895.

(53) Xu, C.; Yu, L.; Zhu, C.; Yu, J.; Cao, Z. Intersystem crossing-branched excited-state intramolecular proton transfer for o-nitrophenol: An ab initio on-the-fly nonadiabatic molecular dynamic simulation. *Sci. Rep.* **2016**, *6*, 26768.

(54) Yue, L.; Yu, L.; Xu, C.; Lei, Y.; Liu, Y.; Zhu, C. Benchmark Performance of Global Switching versus Local Switching for Trajectory Surface Hopping Molecular Dynamics Simulation: Cis↔Trans Azobenzene Photoisomerization. *ChemPhysChem* **2017**, *18*, 1274−1287.

(55) Yue, L.; Liu, Y. Basic Theory and Critical Problems in the Trajectory Surface Hopping Simulations on the Chemiluminescent Reaction of Organic Peroxides. *Chem. J. Chin. Univ.* **2018**, *39*, 2113−2128.

(56) Yue, L.; Liu, Y.; Zhu, C. Performance of TDDFT with and without spin-flip in trajectory surface hopping dynamics: Cis-trans azobenzene photoisomerization. *Phys. Chem. Chem. Phys.* **2018**, *20*, 24123−24139.

(57) Sellner, B.; Barbatti, M.; Lischka, H. Dynamics starting at a conical intersection: Application to the photochemistry of pyrrole. *J. Chem. Phys.* **2009**, *131*, No. 024312.

(58) Verlet, L. Computer ″Experiments″ on Classical Fluids. I. Thermodynamical Properties of Lennard-Jones Molecules. *Phys. Rev.* **1967**, *159*, 98−103.

(59) Verlet, L. Computer ″Experiments″ on Classical Fluids. II. Equilibrium Correlation Functions. *Phys. Rev.* **1968**, *165*, 201−214.

(60) Swope, W. C.; Andersen, H. C.; Berens, P. H.; Wilson, K. R. A computer simulation method for the calculation of equilibrium constants for the formation of physical clusters of molecules: Application to small water clusters. *J. Chem. Phys.* **1982**, *76*, 637−649.

(61) Barbatti, M.; Granucci, G.; Ruckenbauer, M.; Plasser, F.; Pittner, J.; Persico, M.; Lischka, H. *NEWTON-X: a package for Newtonian dynamics close to the crossing seam, version 1.4*; NewtonX, Inc.: www.newtonx.org, 2013.

(62) Thiel, W. *MNDO99 program, version 6.1*; Max-Planck-Institut für Kohlenforschung: Mülheim, Germany, 2007.

(63) Rackers, J. A.; Wang, Z.; Lu, C.; Laury, M. L.; Lagardère, L.; Schnieders, M. J.; Piquemal, J.-P.; Ren, P.; Ponder, J. W. Tinker 8: Software Tools for Molecular Design. *J. Chem. Theory Comput.* **2018**, *14*, 5273−5289.

(64) Nakamura, H.; Truhlar, D. G. Extension of the fourfold way for calculation of global diabatic potential energy surfaces of complex, multiarrangement, non-Born−Oppenheimer systems:Application to HNCO(S_0,S_1). *J. Chem. Phys.* **2003**, *118*, 6816−6829.

(65) Ciscato, L. F. M. L.; Bartoloni, F. H.; Bastos, E. L.; Baader, W. J. Direct Kinetic Observation of the Chemiexcitation Step in Peroxyoxalate Chemiluminescence. *J. Org. Chem.* **2009**, *74*, 8974−8979.

(66) Ding, B.-w.; Naumov, P.; Liu, Y.-J. Mechanistic Insight into Marine Bioluminescence: Photochemistry of the Chemiexcited *Cypridina* (Sea Firefly) Lumophore. *J. Chem. Theory Comput.* **2015**, *11*, 591−599.

(67) Tang, Y.-Q.; Liu, Y.-J. Theoretical study on bioluminescent mechanism and process of Siberian luminous earthworm Fridericia heliota. *J. Photochem. Photobiol., A* **2019**, *380*, 111870.

(68) Cederbaum, L. S. BORN−OPPENHEIMER APPROXIMATION AND BEYOND. In *Conical Intersections: Electronic Structure, Dynamics and Spectroscopy*; first edition; Domcke, W., Yarkony, D. R., Köppel, H., World Scientific Publishing Co. Pte. Ltd.: Singapore, 2004; Vol. *15*, pp. 3−40.

(69) Yue, L.; Lan, Z.; Liu, Y.-J. The Theoretical Estimation of the Bioluminescent Efficiency of the Firefly via a Nonadiabatic Molecular Dynamics Simulation. *J. Phys. Chem. Lett.* **2015**, *6*, 540−548.

(70) Pi, S.; Li, Q.; Yue, L.; Liu, Y.-J. Mechanistic Investigation on Chemiluminescent Formaldehyde Probes. *Chem. − Eur. J.* **2021**, *27*, 5712−5720.